Journal of the European Ceramic Society 21 (2001) 1037–1047

www.elsevier.com/locate/jeurceramsoc

Thermochemistry and microstructures of MgO–C refractories containing various antioxidants

S. Zhang, N.J. Marriott, W.E. Lee *

Department of Engineering Materials, The University of Sheffield, Sheffield S1 3JD, UK

Received 6 July 2000; received in revised form 18 October 2000; accepted 21 October 2000

Abstract

Reactions on firing MgO–C refractories with added Al, Si and B_4C have been predicted by thermodynamic calculations and observations made of microstructures given equivalent treatments. At 1200 and 1500°C, addition of Al leads to generation of Al_4C_3, AlN, Al_2O_3 and magnesium aluminate spinel, MA. Gaseous species, such as Al(g), participate in their formation processes as predicted and suggested by their morphologies. For example, AlN occurs as whiskers and MA as fine precipitates in the matrix and as surface layers on MgO aggregates. Additionally, Al_2O_3 and Al_4C_3 shells occur surrounding porous cores at the location of the original Al particles. At 1200°C, addition of Si leads to formation of SiC, Si_3N_4, SiO_2 and forsterite, M_2S. These phases are still present at 1500°C except for Si_3N_4 which is not thermodynamically stable. Gaseous species such as SiO(g) were also involved in formation of these product phases as predicted and suggested by their morphologies. M_2S occurred as fine precipitates in the matrix and as a layer on MgO aggregate surfaces. SiO_2 formed either directly as a layer on Si particles or indirectly as a shell around a SiC core. Thermodynamic calculations predict that at 1200 and 1500°C B_4C reacts with N_2 from the atmosphere to form BN and/or with CO from the atmosphere to form B_2O_3 which further reacts with MgO to form low melting $3MgO.B_2O_3$, M_3B. M_3B becomes liquid > 1350°C and takes up impurities from MgO and/or graphite raw materials, forming more liquid, which will be detrimental to the refractories corrosion resistance. M_3B was detected in the microstructures but there was no direct evidence of BN formation and its reaction with CO. Gaseous species such as B_2O_3(g) were also involved in M_3B formation.

Keywords: MgO; Carbon; Refractories; Microstructure; Antioxidants

1. Introduction

MgO–C refractories are widely used in both basic oxygen and electric arc primary steelmaking furnaces for their excellent thermal shock resistance and slag resistance. However, due to the presence of carbon, the refractories suffer two main drawbacks, low mechanical strength and poor oxidation resistance. To overcome these, so-called antioxidants are added to the powder batches during brick fabrication.

Antioxidants often used in MgO–C refractories include metals/alloys (such as Al, Si, Mg and Al/Mg alloy), carbides (such as B_4C and SiC), and boron-based compounds (such as CaB_6 and ZrB_2).[1–5] These antioxidants function in different ways during the refractories use. Early thermodynamic analyses on the Al–C–O and Si–C–O systems[6] revealed that Al and SiC (or Si) suppress carbon oxidation in two main ways. Firstly by reducing CO to C, and secondly by decreasing porosity (and so limiting permeation by oxidising gases) via volume expansions and C precipitation accompanying the reaction of Al or SiC(or Si) with CO. Later studies of the Al–C–O–N system[7] revealed that Al either reacts with C to form Al_4C_3 or with N_2 from the atmosphere to form AlN, and the Al_4C_3 and AlN further reduce CO to C and themselves oxidise to become Al_2O_3. The reduction of CO to C contributes to the carbon oxidation inhibition, and the formation of reaction products such as AlN, Al_4C_3 and Al_2O_3 to the improved mechanical strength.[7] Yamaguchi extended his study of the Al–C–O–N system and also examined Si–C–O–N and Zr–C–O–N systems[8] discussing the influence of temperature and partial pressures of CO (or O_2) and N_2 on the stability of metals, carbides and oxides. This work showed that the antioxidants not only act as CO reducing agents, but also encourage the formation of an oxide dense layer

* Corresponding author. Tel.: +44-114-2225474; fax: +44-114-222 5943.

E-mail address: w.e.lee@sheffield.ac.uk (W.E. Lee).

0955-2219/01/$ - see front matter
PII: S0955-2219(00)00308-3

at the hot face, both mechanisms inhibiting carbon oxidation. B_4C, as an additive, reacts with CO to form B_2O_3 which reacts with MgO to form low melting $3MgO.B_2O_3$ (M_3B).[9] B_2O_3 and/or M_3B phases are liquids at high temperatures, their formation blocks open pores and/or covers the carbon surface and thus suppresses its oxidation. For metal alloy additives, the reaction mechanism may be considered as a combination of the mechanism of each component. Depending on the reactivity of each component with CO (or O_2), they will function at a different stage.[10] For example, if an Al/Si alloy is added, the Al in the alloy acts first as the antioxidant. Once the Al is exhausted, Si begins to work as the antioxidant.[10] Later thermodynamic calculations on the behaviour of metal antioxidants predict similar reaction mechanisms to those suggested by Yamaguchi.[11–14]

Thermodynamic calculations cannot only be used to predict the reaction behaviour of antioxidants at high temperatures, but also can assist selection of proper antioxidants for carbon-containing refractories. Their drawback is that they do not provide any information on the microstructural morphology and distribution of each reaction product formed and so cannot reveal the effect of antioxidants on MgO–C bricks microstructure at high temperatures. To fully understand the reaction mechanisms of antioxidants at high temperatures, both thermodynamic analyses and microstructural examination are needed. However, compared with the extensive work on the former, that on the latter,[15] or on both,[16] is limited. Consequently, current understanding of the reaction sequences and microstructural evolution is far from complete. Therefore, in this paper, the high-temperature reaction processes of Al, Si and B_4C in MgO–C refractories have been predicted using the FACT (Facility for Analysis of Chemical Thermodynamics) package,[17] and their influence on the microstructures of the MgO–C bricks has been examined using X-ray diffraction analysis (XRD), scanning electron microscopy (SEM) and energy dispersive spectroscopy (EDS) techniques.

2. Experimental and calculation procedures

2.1. Raw materials and refractories fabrication

Fused magnesia, sintered magnesia, and graphite flake, with chemical compositions shown in Table 1, comprised the basic mix. The following additives (>98% pure) were made individually: 5 wt.% Al, 5 wt.% Si, or 5 wt.% B_4C. 3 wt.% phenolic resin (Borden (UK), Ltd. Southampton, UK) was used as a binder. The basic materials (40 wt.% fused MgO, 40 wt.% sintered MgO and 20 wt.% graphite) and additives were mixed and pressed following the standard commercial practice. Applied compacting pressure was 270 MPa. After pressing, the bricks were cured at 270°C for 1 h. The apparent porosities of the bricks were ~4 vol.%, and the bulk densities ~2.8 g/cm^3.

2.2. Refractories heat-treatment and microstructural characterisation

Cubes (~15×15×15 mm) were cut from the cured bricks, embedded in carbon powder in an alumina crucible (ϕ60×80 mm) with a lid, and heated to 1200 and 1500°C respectively, at 2°C/min. Soaking times at both temperatures were 3 h. After heating, the furnace was allowed to cool to room temperature at about 2°C/min. The fired samples were then mounted in cold setting resin and standard ceramographic grinding and polishing techniques used. The polished and fracture surfaces of all samples were carbon-coated and examined in back-scattered electron (BEI) and secondary electron imaging (SEI) modes in a Camscan Series 2A SEM. EDS analysis was performed in the Camscan using a LINK detector and AN10000 package and in the JEOL 6400 using its windowless EDS detector. XRD (Philips powder diffractometer 1710 with Ni filtered CuK_α radiation) was also conducted to assist identification of the phases formed in the microstructures.

2.3. Thermodynamic calculation

Equilibrium thermodynamic calculations were performed using the FACT package.[17] The Gibbs energy minimization module EQUILIBRIUM was used together with the FACT databases. The atmosphere in the carbon powder bed is approximately 35% CO + 65%N_2,[14] so this composition was used in all calculations to model the atmosphere surrounding the samples. A small amount of Ar gas (5 wt.%) was included in the calculations to ensure the calculations converged but without affecting the reaction processes. In the case of B_4C additions, the soln-slag database was used for MgO–B_2O_3 melt. As will be discussed elsewhere,[18] at high temperatures, the impurities (~3 wt.%) in the bricks may interact with

Table 1
Chemical composition of the basic raw materials (wt.%)

	MgO	C	SiO_2	Al_2O_3	Fe_2O_3	CaO	Mn_3O_4	B_2O_3
Fused magnesia	97.55	–	0.37	0.03	0.06	1.86	0.11	0.004
Sintered magnesia	96.88	–	0.48	0.06	0.14	2.20	0.14	0.008
Graphite flake	0.13	96.80	1.50	0.55	0.73	0.15	–	–

grain phases and antioxidants, forming small volumes of liquid, which may affect the high-temperature properties. However, this liquid is not believed to affect the primary reaction mechanisms of the antioxidants and the resulting microstructural evolution so that it was not included in the thermodynamic calculations described here. The calculations considered 100 g of refractory and examined the changes in predicted phase constitutions consequent on successive additions of the atmosphere (increase of A/R). When $A/R = 1.0$, the calculation was carried out with 100 g refractory and 10 g atmosphere. The results were plotted as log mole number of species versus A/R. Varying A provides a reservoir of gas to interact with the refractory, varying pO_2 in a way which relates to the gas phase present at the brick surface during the experiments.

3. Results

3.1. Thermodynamic prediction of phase changes at high temperatures

Fig. 1 shows predicted phase changes of the Al added sample at 1200°C with A/R. Al metal is not stable at this temperature. When A/R is close to zero, the amount of Al_4C_3 is high, whereas AlN and $MgAl_2O_4$ (MA) spinel contents are close to zero. With increasing A/R, the Al_4C_3 content decreases whereas AlN and MA contents increase. When A/R increases to ~0.32, the amount of Al_4C_3 abruptly drops to zero. Thereafter, on further increasing A/R, MA still increases, whereas AlN gradually decreases. The amount of carbon (C) increases slightly with increasing A/R, especially when the A/R is below ~0.32 (i.e. before Al_4C_3 disappears). When A/R is lower than ~0.32, the partial pressures of N_2 and CO are $< 10^{-6}$ atm. The partial pressure of Mg(g) is low ($< 10^{-5}$ atm). Predicted phase changes at 1500°C (Fig. 2) are similar to those at 1200°C although the partial pressure of Mg(g) is higher (10^{-3}–10^{-4} atm) than at 1200°C.

In the Si added sample at 1200°C (Fig. 3), Si is not a stable phase and when A/R is close to zero, the SiC content is high whereas Si_3N_4 and Mg_2SiO_4 (M_2S) forsterite contents are very low. With increasing A/R, SiC drops off and Si_3N_4 and M_2S increase. When A/R increases to ~0.42, the amount of SiC abruptly decreases to zero. Thereafter, M_2S still increases with A/R whereas Si_3N_4 decreases. Similar to the Al addition, the C content increases slightly with increasing A/R, especially when A/R is below ~0.42 (i.e. before SiC disappears). When A/R is lower than ~0.43, the partial pressures of N_2 and CO are $< 10^{-6}$ atm. The partial pressure of Mg(g) is also low ($< 10^{-5}$ atm) at this temperature. At 1500°C, the predicted phase changes are somewhat different (Fig. 4). Si and Si_3N_4 are not stable in the system and with increasing A/R, SiC decreases whereas M_2S increases. Partial pressures of Mg(g) ($> 10^{-4}$ atm) and SiO(g) (10^{-5}–10^{-4} atm) become significant at this temperature.

In the B_4C added sample at 1200°C with increasing A/R, B_4C content decreases whereas BN and M_3B increase (Fig. 5). When A/R increases to ~0.66, the B_4C

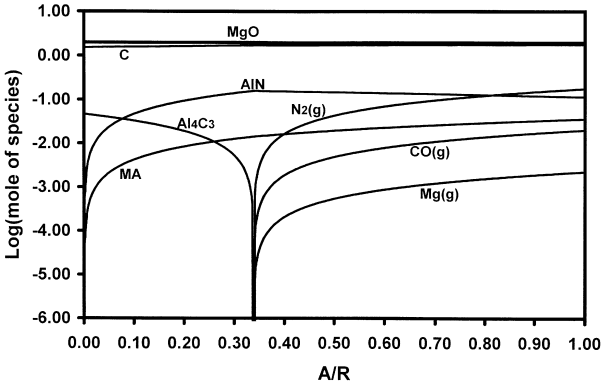

Fig. 2. Phase changes of MgO–C brick containing 5 wt.% Al at 1500°C with A/R.

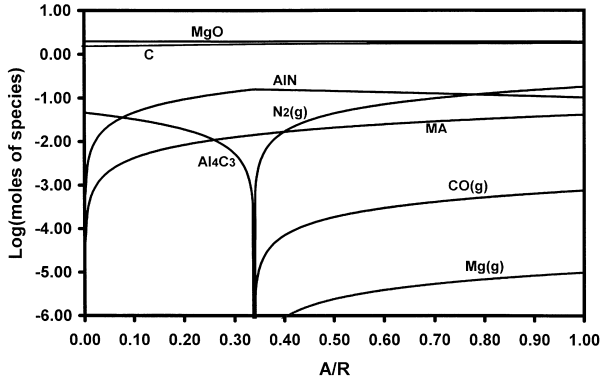

Fig. 1. Phase changes of MgO–C brick containing 5 wt.% Al at 1200°C with A/R.

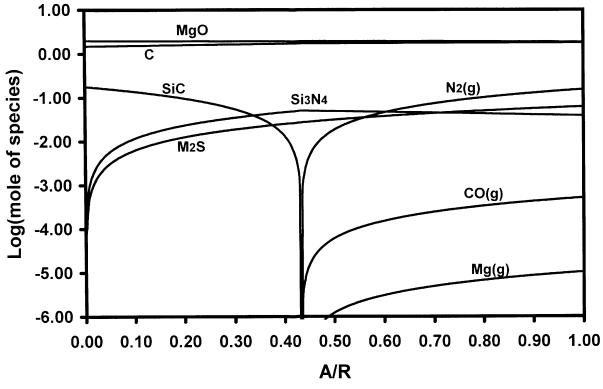

Fig. 3. Phase changes of MgO–C brick containing 5 wt.% Si at 1200°C with A/R.

disappears, and then with increasing A/R, the amount of M_3B increases gradually whereas BN decreases slightly. With increased temperature (1500°C), similar phase changes are predicted (Fig. 6), although at this temperature, a magnesioborate liquid appears. With $A/R \sim 0.62$, the B_4C disappears, and with increasing A/R, the BN and liquid phase contents both decrease slightly. The Mg (g) partial pressures (10^{-5}–10^{-4}atm) at this temperature are much higher than at 1200°C ($< 10^{-6}$ atm).

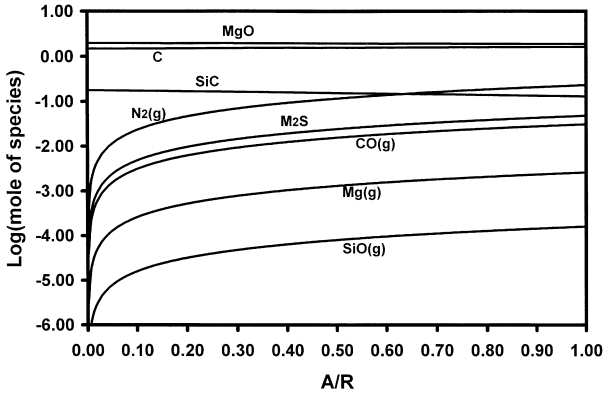

Fig. 4. Phase changes of MgO–C brick containing 5 wt.% Si at 1500°C with A/R.

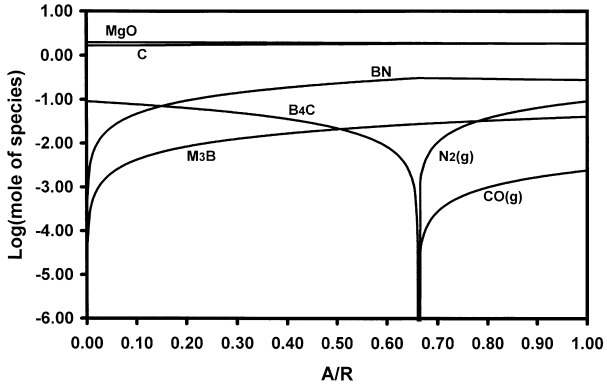

Fig. 5. Phase changes of MgO–C brick containing 5 wt.% B_4C at 1200°C with A/R.

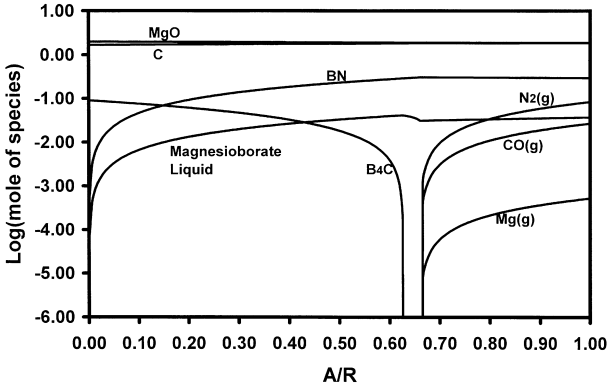

Fig. 6. Phase changes of MgO–C brick containing 5 wt.% B_4C at 1500°C with A/R.

3.2. Microstructures

3.2.1. As-cured microstructure

Fig. 7 shows typical BEI microstructures of the MgO–C samples after curing for 1 h at 270°C. Between the larger angular MgO grains (> 300 μm, light gray con-

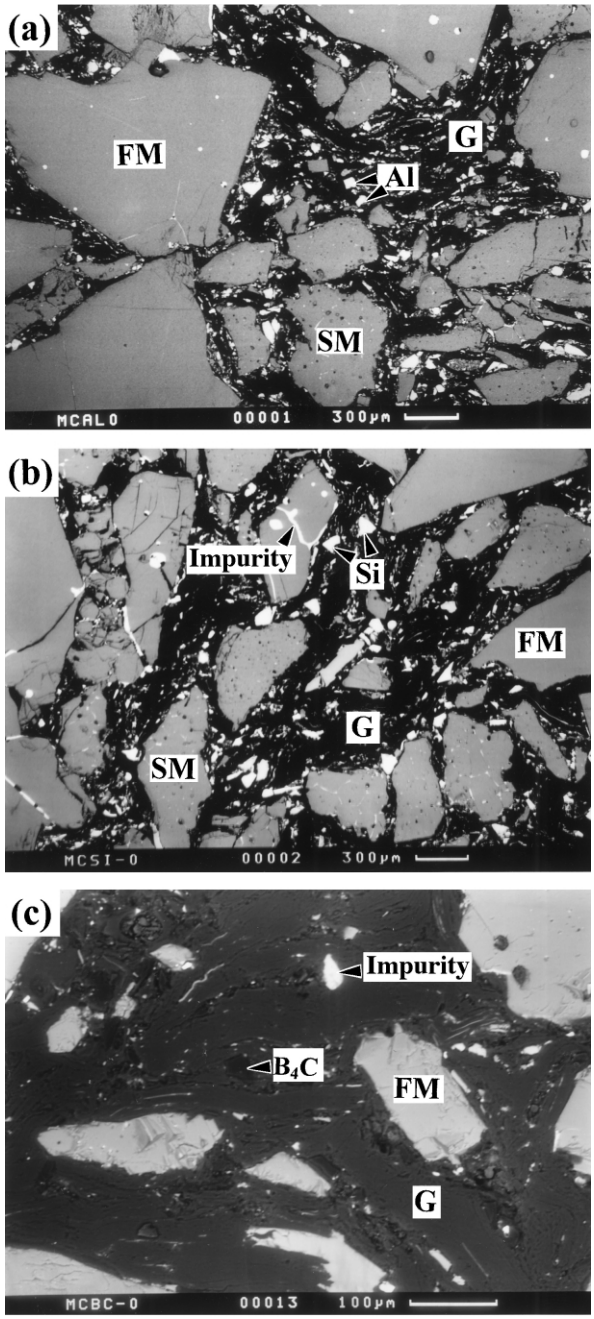

Fig. 7. BEI of MgO–C samples after curing for 1 h at 270°C. (a) Al addition; (b) Si addition; (c) matrix part of the B_4C added sample. FM; fused magnesia, SM; sintered magnesia, G; graphite.

trast), is the matrix composed mainly of graphite (dark contrast), fine MgO (< 50 μm, light gray contrast) and the antioxidants (white angular Al or Si particles in Fig. 7a or b, or black angular B_4C grain in Fig. 7c). A few Fe-containing silicate impurities (bright contrast) were also found between the graphite or inside some MgO aggregates. The impurities were from the MgO and graphite raw materials and though their contrast was similar to that of the Al or Si metal additives, they could be easily distinguished by EDS.

3.2.2. Fired microstructure

3.2.2.1. With Al additive. Samples heated at 1200°C (Fig. 8) reveal only a few unreacted white angular Al crystals remaining in the matrix. The morphologies of the product phases (Al_4C_3 and Al_2O_3) formed in the matrix are revealed at higher magnification (Fig. 9). All were spheroidal located presumably at the site of the original Al metal. Some of these consisted of an Al_2O_3 shell surrounding an Al_4C_3 core (Fig. 9a) others were solid Al_4C_3 (Fig. 9b), and others were an Al_2O_3 shell containing Al particles (white contrast in Fig. 9c). Central voids or pores formed the cores inside Al_4C_3 (Fig. 9a) or Al_2O_3 shells (Fig. 9c). Besides Al_4C_3 and Al_2O_3, AlN whiskers formed between the graphite flakes and on Al_4C_3 grain surfaces (Fig. 10). At this temperature, cuboidal MA spinel was only occasionally observed (Fig. 11).

The microstructures after 3 h at 1500°C were similar to those at 1200°C, although little Al remained and more spinel had formed (Fig. 12). Higher magnification (Fig. 13) reveals that as well as in the matrix much MA precipitated on the large MgO aggregate surfaces. Al_4C_3 cores and Al_2O_3 shells were also found, and EDS analyses revealed small amounts of MA in the Al_2O_3 shells.

3.2.2.2. With Si additive. After 3 h at 1200°C, much unreacted Si still remained in the brick matrix, although product phases such as SiC, SiO_2 and M_2S had begun to form (Fig. 14). Higher magnification of the matrix (Fig. 15) reveals that a SiO_2 shell formed on the SiC or occasionally on the unreacted Si surface. Additionally, Si_3N_4 whiskers coexisting with SiC grains were observed (Fig. 16). At this temperature, M_2S was only occasionally found on some MgO grain surfaces. When the temperature increased to 1500°C, only a little unreacted Si remained and more SiC and SiO_2 phases formed in the matrix (Fig. 17). Unlike at 1200°C, Si_3N_4 was only

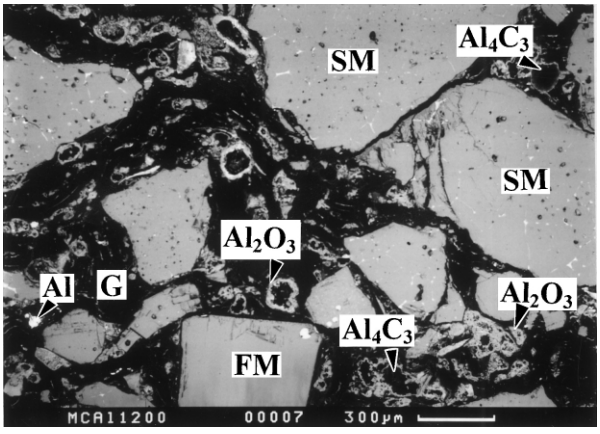

Fig. 8. BEI of Al added sample after 3 h at 1200°C. Al_4C_3 with an Al_2O_3 shell was found in the matrix.

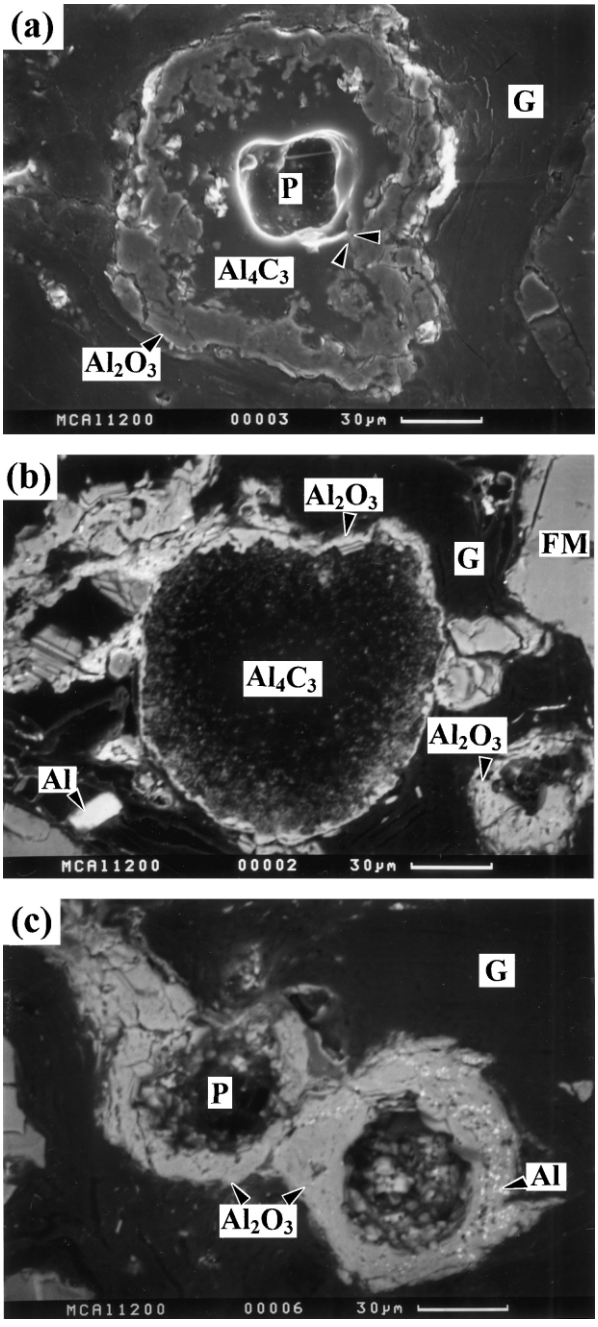

Fig. 9. Microstructural morphologies of Al_4C_3 and Al_2O_3 formed in the matrix of Al added sample after 3 h at 1200°C. (a) An Al_4C_3 core with a pore in its center, was covered by an Al_2O_3 shell (SEI); (b) a solid Al_4C_3 grain was covered by an Al_2O_3 shell (BEI); (c) an Al_2O_3 shell with Al particles, enclosed a pore (BEI). P, pore.

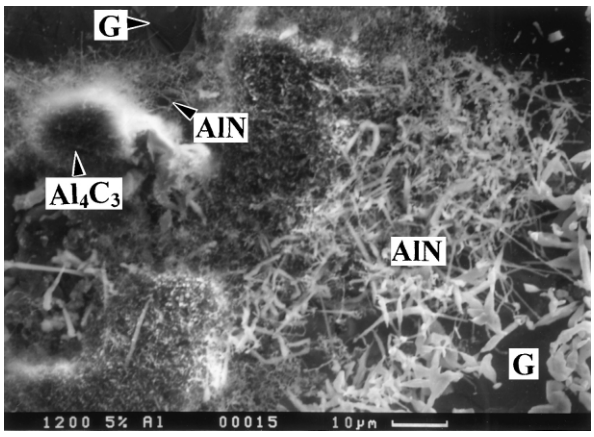

Fig. 10. AlN whiskers formed in the Al added sample after 3 h at 1200°C (SEI). Note AlN formed between graphite flakes and on Al_4C_3 grain surfaces.

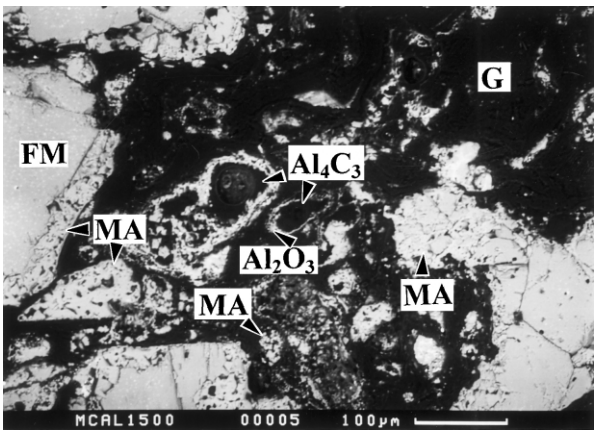

Fig. 13. Higher magnification BEI of the sample shown in Fig. 12, showing more MA spinel precipitated in the matrix and on the MgO aggregate surfaces. Al_4C_3 cores and Al_2O_3 shells were also found.

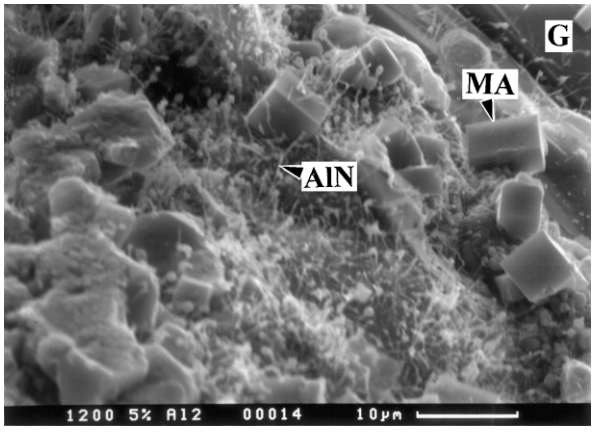

Fig. 11. MA spinel was occasionally found on the fracture surface of the Al added sample after 3 h at 1200°C (SEI).

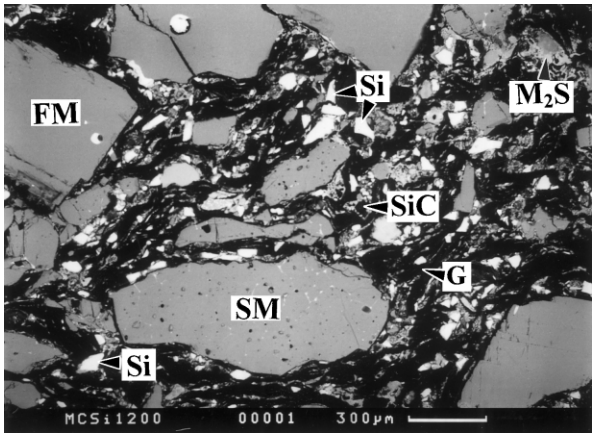

Fig. 14. BEI of the Si added sample after 3 h at 1200°C. Many unreacted Si grains still remained in the sample, although SiC and SiO_2 began to appear. Mg_2SiO_4 forsterite (M_2S) was occasionally found in the sample.

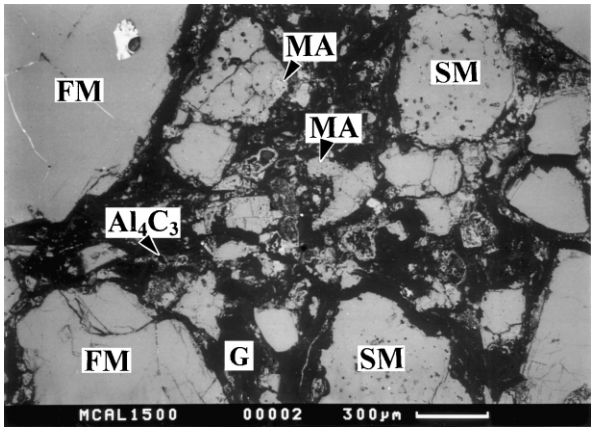

Fig. 12. BEI of the Al added sample after 3 h at 1500°C, showing the formation of Al_4C_3 and MA spinel.

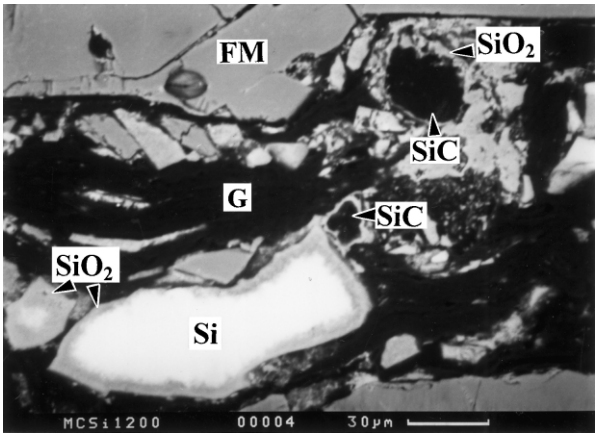

Fig. 15. Higher magnification BEI of the matrix shown in Fig. 14, showing SiO_2 shell covered SiC or unreacted Si grain.

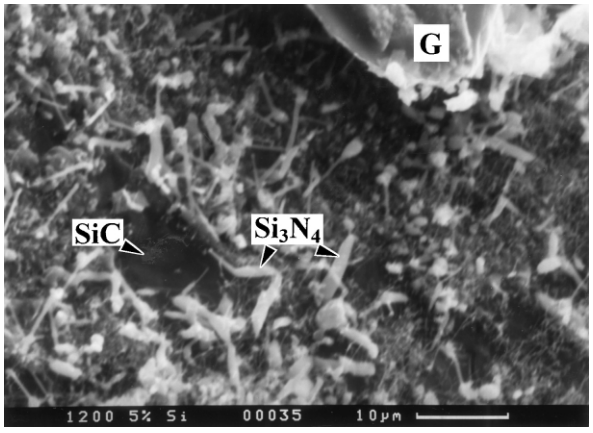

Fig. 16. Si_3N_4 whiskers observed on the fracture surface of the Si added sample after 3 h at 1200°C (SEI).

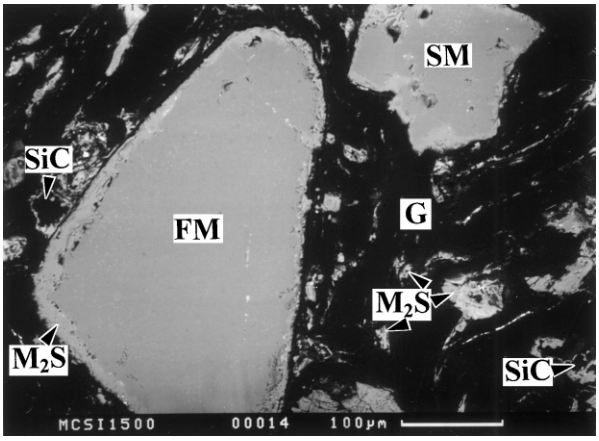

Fig. 18. M_2S precipitated in the matrix and on the MgO aggregate surfaces of the sample shown in Fig. 17 (BEI).

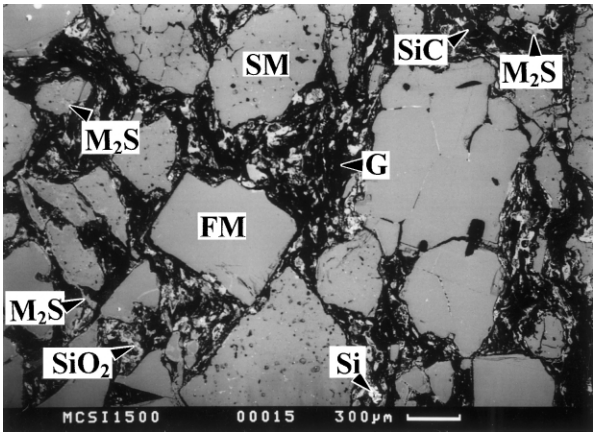

Fig. 17. BEI of the Si added sample after 3 h at 1500°C. Only a little unreacted Si remained in the sample. More M_2S was found, although its morphology could be seen more clearly from Fig. 18.

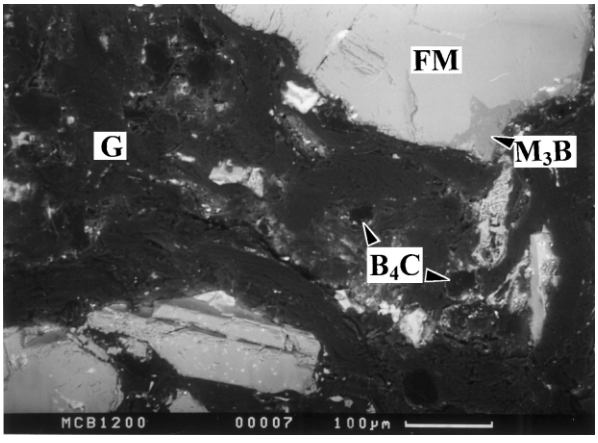

Fig. 19. BEI of the B_4C added sample after 3 h at 1200°C. $3MgO.B_2O_3$ (M_3B) phase began to form on the MgO aggregate surface.

occasionally detected (not shown), and more M_2S was detected in the matrix and on the large MgO aggregate surfaces (Fig. 18).

3.2.2.3. With B_4C additive. After 3 h at 1200°C, unreacted B_4C (black angular grain) could still be observed. However, unlike with Al and Si additions, there was no obvious oxide shell covering the unreacted B_4C. Dark gray laths of M_3B were located on some MgO aggregate surfaces (Fig. 19). When the temperature was increased to 1500°C, a few unreacted B_4C grains still remained in the matrix, but a greater amount of M_3B was observed both in the matrix and on the MgO aggregate surfaces (Fig. 20). Some silicate phase (white contrast) coexisting with the M_3B was also observed. EDS revealed that it mainly comprising Mg, Ca, B, Si and a small amount of Fe.

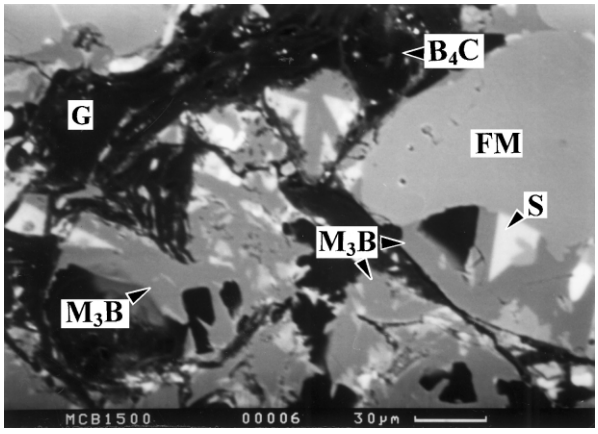

Fig. 20. BEI of the B_4C added sample after 3 h at 1500°C. Greater amount of M_3B formed in the matrix and on the MgO aggregate surfaces. S = silicate.

4. Discussion

4.1. Comparison of thermodynamic predictions and microstructural observations

4.1.1. With Al additive

Thermodynamic calculations indicate (Figs. 1 and 2), when A/R is close to zero, Al_4C_3 is the main stable solid phase along with MgO and C. Physically this corresponds in the real sample to the situation when the atmosphere has not diffused into the sample. In this case Al initially reacted with C to form Al_4C_3 [Reaction (1)].

$$4Al(s,l) + 3C(s) = Al_4C_3(s) \quad (1)$$

When A/R is between 0 and ~0.32, the partial pressures of N_2 and CO are very low ($<10^{-6}$ atm), and with increasing A/R in this range, the amount of Al_4C_3 decreases and that of AlN, MA and C increase (Figs. 1 and 2), indicating that with more gaseous diffusion into the sample, the Al_4C_3 reacted with N_2 from the atmosphere to form AlN [Reaction (2)] or was directly oxidised by CO to Al_2O_3 [Reaction (3)] which further reacted with MgO in the brick to form MA [Reaction(4)].

$$Al_4C_3(s) + 2N_2(g) = 4AlN(s) + 3C(s) \quad (2)$$

$$Al_4C_3(s) + 6CO(g) = 2Al_2O_3(s) + 9C(s) \quad (3)$$

$$Al_2O_3(s) + MgO(s) = MgAl_2O_4(s) \quad (4)$$

The formation of Al_2O_3 on the surfaces of Al_4C_3 cores (Fig. 9a) or as porous shells (Fig. 9c) and the formation of MA (Figs. 11–13) verified the oxidation of Al_4C_3, and the precipitation of AlN whiskers on the Al_4C_3 grain surface (Fig. 10) indicated the transformation of Al_4C_3 to AlN. Moreover, the morphologies of AlN (whiskers, Figs. 10 and 11) and MA (precipitating on the MgO aggregate surfaces, Figs. 12 and 13). suggested that gaseous species such as Al(g) were involved in the net reaction processes indicated by Reactions (2)–(4). Yamaguchi[7] suggested that the partial pressure of Al (g) in equilibrium with Al_4C_3 is high, therefore, before the Al_4C_3 reacted with the atmosphere, Al(g) evaporated from it (Reaction(5)) and diffused throughout the sample. Later, as the atmosphere diffuses around the sample, the Al(g) either reacted with N_2, leading to precipitation of AlN whiskers [Reaction (6)], or reacted with MgO and CO surrounding the MgO aggregate, leading to the precipitation of MA on the MgO aggregate surfaces [Reaction (7)]. At 1200°C, only a small amount of MA formed in the brick, indicating that kinetic factors were hindering its formation [e.g. Reaction (7)]. When the temperature was increased to 1500°C, the partial pressure of Al(g) in equilibrium with Al_4C_3 increases[7], and that of Mg(g) also becomes significant due to the MgO–C reaction[19] [Reaction (8)] (Fig. 2). Therefore, besides the gas–solid reaction process [Reaction (7)], a gas–gas reaction process [Reaction (9)] began to contribute to the MA formation.

$$Al_4C_3(s) = 4Al(g) + 3C(s) \quad (5)$$

$$2Al(g) + N_2(g) = 2AlN(s) \quad (6)$$

$$2Al(g) + MgO(s) + 3CO(g) = MgAl_2O_4(s) + 3C(s) \quad (7)$$

$$MgO(s) + C(s) = Mg(g) + CO(g) \quad (8)$$

$$2Al(g) + Mg(g) + 4CO(g) = MgAl_2O_4(s) + 4C(s) \quad (9)$$

Reaction (7) was considered to be responsible for precipitation of MA on the MgO aggregate surfaces (Figs. 12–13), and Reaction (9) for precipitation of MA in the matrix (Fig. 13) due to easier transport of the vapour species, both contributing to greater formation of MA at 1500°C.

Calculations indicate that when A/R increases to ~0.32, the amount of Al_4C_3 abruptly decreases to zero, thereafter further increasing A/R, the amount of MA still increases whereas that of AlN decreases. In the real sample, this means that when this amount of atmosphere diffused into the refractory, all of the Al_4C_3 would be changed to AlN according to Reaction (2) and/or oxidised to Al_2O_3 according to Reaction(3). Further increasing the CO and N_2 vapour contents of the atmosphere, leads to the AlN, instead of Al_4C_3, being oxidised to Al_2O_3 [Reaction (10)] which further reacted with MgO to MA [Reaction (4)].

$$2AlN(s) + 3CO(g) = Al_2O_3(s) + N_2(g) + 3C(s) \quad (10)$$

There was no direct microstructural evidence for the occurrence of Reaction (10). This may be due to kinetic factors so that Al_4C_3 still remained (Figs. 8, 9, 12 and 13), therefore, before it disappeared, the AlN was a stable phase (Figs. 1 and 2).

Another notable feature of the Al added sample is the formation of the Al_4C_3 cores and/or Al_2O_3 shells in the matrix (Fig. 9a and c). The following mechanism was suggested[20] for Al_4C_3 shell and pore formation: Al initially reacts with C to form an Al_4C_3 shell and Al(l) is enclosed in the shell; next cracks form in the weakest parts of the shell due to the volume expansion mismatch between Al and Al_4C_3, and finally Al(g) evaporates from the Al(l) and escapes the shell through the cracks and thus leaving a pore in the centre. However, careful examination of the microstructures shown in Fig. 9 found that this mechanism cannot explain some features observed here. For example, it cannot explain why for two Al grains with similar size, a pore formed in one (Fig. 9a) but not in another (Fig. 9b). Based on the

microstructural results in this study, the shell and pore formation mechanisms are suggested to be as follows. At high temperatures, Al reacts with C to form an Al_4C_3 shell [Reaction (1)] or occasionally reacts with CO directly to form an Al_2O_3 shell [Reaction (11)].

$$2Al(l) + 3CO(g) = Al_2O_3(s) + 3C(s) \quad (11)$$

If the Al_4C_3 shell forms, and if it is not quickly oxidised by CO, it will continue growing and finally become a solid Al_4C_3 grain (Fig. 9b). On the other hand, if it is quickly oxidised by CO, because the oxidation [Reaction (3)] leads to a large volume expansion (~93.5%), the Al_2O_3 shell has low density and may contain cracks or micropores (see Fig. 9a). Consequently, when the oxidation frontier (the Al_2O_3 shell) reaches the Al(l) enclosed in the Al_4C_3 shell (see the places indicated by two arrows in Fig. 9a), the Al(g) will evaporate and get out through the cracks or micropores in the Al_2O_3 shell and thus leave a pore in the centre (Fig. 9a). The mechanism is similar for formation of an Al_2O_3 shell, because the Al(l) oxidation reaction [Reaction (11)] is also accompanied by a large volume expansion (~142%), leading to the formation of a porous and crack-containing Al_2O_3 shell (Fig. 9c).

4.1.2. With Si additive

As shown in Fig. 3, at 1200°C, when the CO and N_2 level is close to zero, SiC is the main stable solid phase along with MgO and C. In the real sample, this means that before the atmosphere diffused into the sample, the Si initially reacted with C to form SiC [Reaction (12)].

$$Si(s) + C(s) = SiC(s) \quad (12)$$

When A/R is between 0 and ~0.42, the partial pressures of N_2 and CO are very low, and with increasing A/R in this range, the amount of SiC decreases and Si_3N_4 and M_2S levels increase (Fig. 3), indicating that with more CO and N_2 diffused, the SiC reacted with N_2 from the atmosphere to form Si_3N_4 [Reaction (13)] or with CO (g) from the atmosphere to form SiO_2 [Reaction (14)] which further reacted with MgO to form M_2S [Reaction (15)].

$$3SiC(s) + 2N_2(g) = Si_3N_4(s) + 3C(s) \quad (13)$$

$$SiC(s) + 2CO(g) = SiO_2(s) + 3C(s) \quad (14)$$

$$SiO_2(s) + 2MgO(s) = Mg_2SiO_4(s) \quad (15)$$

When A/R increases to ~0.42 at 1200°C, all of the SiC is changed to Si_3N_4 and/or SiO_2, so the amount of SiC abruptly decreases to zero, thereafter, the amount of M_2S still increases whereas that of Si_3N_4 decreases (Fig. 3). This indicates that after all of the SiC is changed to Si_3N_4 and/or SiO_2, the Si_3N_4 will begin to be oxidised to SiO_2 [Reaction (16)] which further reacts with MgO to form M_2S [Reaction (15)].

$$Si_3N_4(s) + 6CO(g) = 3SiO_2(s) + 6C(s) + 2N_2(g) \quad (16)$$

SiC, Si_3N_4 and SiO_2 were detected in the microstructures (Figs. 14–16). M_2S was also detected, although for kinetic reasons, it was only found occasionally. The formation of a SiO_2 shell on the SiC (Fig. 15) verified the occurrence of Reaction(14), and the formation of Si_3N_4 on the SiC grain (Fig. 16) supported the process indicated by Reaction (13). A SiO_2 shell was also occasionally found on the unreacted Si (Fig. 15), indicating that occasionally Si could be directly oxidised to SiO_2. For similar reasons to those given for the Al addition case for reaction between AlN and CO [Reaction (10)], there was no microstructural evidence for Reaction (16), although the reaction is predicted by the thermodynamic calculation (Fig. 3).

When the temperature increases to 1500°C, thermodynamic calculations (Fig. 4) reveal that Si_3N_4 is not a stable phase. This means that even if Si_3N_4 forms at low temperature (e.g. upon heating), it will convert to SiC again when the temperature reaches 1500°C, Si_3N_4 occasionally detected in the microstructure (not shown) most likely precipitated on cooling. As predicted and shown in Fig. 4, before the CO and N_2 atmosphere diffused into the refractory, Si reacted with C to form SiC. With increasing levels of CO and N_2 diffusing into the sample, the amount of SiC decreases and that of M_2S increases, indicating that SiC reacted with CO from the atmosphere to form SiO_2 [Reaction (14)] which further reacted with MgO to form M_2S [Reaction (15)]. The microstructures (Figs. 17 and 18) confirmed the formation of SiC, SiO_2 and M_2S. The precipitation of M_2S in the matrix and on the large MgO aggregate surfaces (Fig. 18), indicates that gaseous species are involved in its formation. As shown in Fig. 4, the partial pressures of SiO(g) [from Reaction (17)] and Mg(g) [Reaction (8)] become significant at 1500°C. Therefore, similar to the MA formation in the Al added samples, M_2S could form via both gas-solid [Reaction (18)] and gas-gas reaction processes [Reaction (19)].

$$SiC(s) + CO(g) = SiO(g) + 2C(s) \quad (17)$$

$$SiO(g) + 2MgO(s) + CO(g) = Mg_2SiO_4(s) + C(s) \quad (18)$$

$$SiO(g) + 2Mg(g) + 3CO(g) = Mg_2SiO_4(s) + 3C(s) \quad (19)$$

Reaction (18) is likely to be responsible for precipitation of M_2S on the MgO aggregate surfaces, and Reaction (19) for precipitation of M_2S in the matrix (Fig. 18). Both

contributed to the formation of a greater amount of M_2S in the brick at this temperature (Figs. 17 and 18).

In contrast to the Al added samples, no pores were found in the centre of SiO_2 or SiC shells (Fig. 15). This may be because the partial pressure of Si(g) in equilibrium with Si(l, s) is very low ($<10^{-7}$ atm) at the test temperatures,[7] so even if the cracks formed in the shell, the evaporation of Si(g) from the Si metal could not lead to formation of a pore inside the shell.

4.1.3. With B_4C additive

Thermodynamic calculations (Fig. 5) show that at 1200°C, with increasing CO and N_2 atmosphere, the amount of B_4C decreases while BN and M_3B levels increase, indicating that with more CO and N_2 atmosphere present, B_4C reacted with N_2 to form BN [Reaction (20)] or with CO to form B_2O_3 [Reaction (21)] which further reacted with MgO to form M_3B [Reaction (22)].

$$B_4C(s) + 2N_2(g) = 4BN(s) + C(s) \quad (20)$$

$$B_4C(s) + 6CO(g) = 2B_2O_3(l) + 7C(s) \quad (21)$$

$$B_2O_3(l) + 3MgO(s) = 3MgO.B_2O_3(s) \quad (22)$$

When A/R increases to ~0.66, B_4C disappears, thereafter, on further increasing A/R, BN content decreases slightly and that of M_3B increases slightly, indicating that after B_4C disappears, a small amount of BN reacts with CO from the atmosphere to form B_2O_3 [Reaction (23)] which further reacts with MgO to form M_3B [Reaction (22)].

$$2BN(s) + 3CO(g) = B_2O_3(l) + 3C(s) + N_2(g) \quad (23)$$

The microstructure confirmed the formation of M_3B (Fig. 19). However, it did not provide any direct evidence of BN formation and its reaction with CO. The possible reasons were (1) kinetic factors might be hindering Reaction (20), so the BN content is very low; and (2) its crystal size might be too small to observe in a conventional SEM.

Similar phase changes at 1500°C were predicted by thermodynamic calculations (Fig. 6), although a magnesioborate liquid appears. Another discrepancy in the prediction is that after B_4C disappears, the amounts of BN and liquid both decrease. The reasons for this are not clear, although it could be due to reduction of MgO in the liquid by C. M_3B was also observed in the microstructure (Fig. 20), however, because its melting point is ~1350°C, it likely precipitated from the liquid on cooling. Some Fe containing Mg borosilicates (white contrast) coexisting with the M_3B were also found, suggesting that at 1500°C, the Mg borate liquid predicted by thermodynamic calculation (Fig. 5) took up some silicate impurities from the MgO grain and graphite, increasing the volume of liquid formed.

The partial pressure of boron-containing vapours such as $B_2O_3(g)$ in equilibrium with $B_2O_3(l)$ is high,[9] so after B_2O_3 formed on the B_4C surface [Reaction (21)], it quickly evaporates. It was for this reason that there was no obvious oxide shell on the unreacted B_4C grain (Fig. 19). The evaporation of boron-containing gaseous species was also responsible for the precipitation of M_3B in the matrix and on the MgO aggregate surfaces (Figs. 19 and 20). Since the mechanisms will be similar to the precipitation of MA or M_2S considered above, they will not be considered further.

4.2. Kinetic constraint

The calculations used in this study are for thermodynamic equilibrium but the microstructures observed clearly demonstrate the kinetic constraints occurring in practice. Reactions between solid oxides [e.g. reactions (4) and (15)] are likely to be slow due to the low diffusivities at the temperatures of the experiments. However, the melting of Al and Si will accelerate any reactions involving them as will the formation of B_2O_3-containing liquid, the latter being particularly fluid and penetrative. Reactions involving gases are likely to be fast and less kinetically hindered. The influence on the corrosion resistance of the microstructures resulting from interaction of additives with MgO–C will be considered in a separate publication.[21]

5. Summary

The reaction processes of Al, Si and B_4C added to MgO–C refractories have been predicted by thermodynamic calculation and compared with microstructural observations. The main results are summarised as follows.

At high temperatures, Al reacts with graphite and/or N_2 to form Al_4C_3 and/or AlN, although occasionally it is oxidised directly to Al_2O_3 by CO. The Al_4C_3 formed reacts with N_2 to form AlN whiskers and/or with CO to form Al_2O_3 which reacts with MgO to form MA. Although there is no direct microstructural evidence, the thermodynamic calculations predict that after Al_4C_3 disappears, AlN will react with CO to form Al_2O_3 which reacts with MgO to form MA. Gaseous species such as Al(g) are involved in the above reaction processes, and explain the different morphologies of the reaction products such as AlN (whiskers) and MA(precipitated on large MgO aggregate surfaces). The proportion of MA is much greater after 3 h at 1500°C than after 3 h at 1200°C. Al_4C_3 or Al_2O_3 shells with pores in their centres form in the matrix. After formation of an Al_4C_3 core, if it is not quickly oxidised by CO, it will

continue growing and finally become a solid Al_4C_3 grain, however, if it is quickly oxidised by CO, because the oxidation reaction leads to a large volume expansion (~93.5%), the Al_2O_3 shell is not dense and may contain some cracks or micropores. When the oxidation frontier reaches the Al(l) enclosed in the Al_4C_3 shell, the Al(g) will evaporate and escape from the shell through the cracks or micropores in the Al_2O_3 shell leaving a pore in the centre. In the case of the Al_2O_3 shell, the mechanism is similar, because the shell is also not dense and may contain some cracks or micropores due to a large volume expansion (~142%) accompanying the reaction of Al with CO.

At 1200°C, Si reacts with graphite and/or N_2 to form SiC and/or Si_3N_4, although occasionally it is directly oxidised to SiO_2 by CO. The SiC reacts with N_2 to form Si_3N_4 or with CO to form SiO_2 which further reacts with MgO to form M_2S. Although there is no direct microstructural evidence, thermodynamic calculation reveals that after SiC disappears, Si_3N_4 will react with CO to form SiO_2 which then reacts with MgO to form M_2S. At 1500°C, Si_3N_4 is not thermodynamically stable, so Si_3N_4 occasionally detected in the microstructure most likely precipitated on cooling. At this temperature the SiC formed from reaction between Si and C, reacts with CO to form SiO_2 which reacts with MgO to form M_2S. Gaseous species such as SiO(g) involved in the above reaction processes, explain the different morphologies of the reaction products such as M_2S (precipitated on the large MgO surfaces) in the brick.

Thermodynamic calculation predicts that at high temperatures B_4C reacts with N_2 from the atmosphere to form BN and/or with CO from the atmosphere to form B_2O_3 which further reacts with MgO to form low melting M_3B. The M_3B becomes liquid when the temperature is higher than its melting point (~1350°C), it takes up impurities from MgO and/or graphite raw materials, forming more liquid in the brick, which will be detrimental to the corrosion resistance. The microstructures confirm the formation of M_3B, but have not provided any direct evidence of BN formation and its reaction with CO, although they are predicted by thermodynamic calculations. Gaseous species such as B_2O_3(g) involved in the M_3B formation, are consistent with precipitation of M_3B on the large MgO aggregate surfaces.

Acknowledgements

We would like to thank the EPSRC (Research Grant GR/L31647), Baker Refractories (UK), Vesuvius KSR and British Steel (now Corus) for financial support.

References

1. Taffin, C. and Poirier, J., The reaction of metal additives in MgO–C and Al_2O_3–C refractories. *Interceram*., 1994, **43**, 454–460.
2. Brant, P. O. R. C., Limm, W. A. and Grocener, C. A., Development of high erosion and corrosion resistant MgO–C Bricks for BOF application. In: UNITECR'93 Proceedings, ALAFAR, Sao Paulo, Brazil, 1993, pp. 462–71.
3. Lubaba, N. G., Rand, B. and Brett, N. H., Microstructure and strength of MgO-carbon composite refractory materials. *Br. Ceram. Trans. J*., 1989, **89**, 47–54.
4. Hayashi, S., Takanaga, S., Takahashi, H. and Watanabe, A., Behaviour of boric compounds added in MgO–C bricks. *Taikabutsu Overseas*, 1991, **11**, 12–19.
5. Hanagiri, S., Harada, T. and Fugihara, S., Effects of the addition of metal and CaB_6 to magnesia carbon bricks for converters. *Taikabutsu Overseas*, 1993, **13**, 20–27.
6. Yamaguchi, A., Behaviour of SiC and Al added to carbon-containing refractories. *Taikabutsu Overseas*, 1984, **4**(3), 14–18.
7. Yamaguchi, A., Thermochemical analysis for reaction processes of aluminum and aluminum-compounds in carbon-containing refractories. *Taikabutsu Overseas*, 1987, **7**(2), 4–13.
8. Yamaguchi, A., Affects of oxygen and nitrogen partial pressure on stability of metal, carbide, nitride, and oxide in carbon-containing refractories. *Taikabutsu Overseas*, 1987, **7**(1), 11–16.
9. Yamaguchi, A., Behaviour of boron carbide added to carbon-containing refractories. *Taikabutsu*, 1984, **36**(10), 558–563.
10. Yamaguchi, A. and Tanaka, H., Role and behaviour of non-oxide compounds added to carbon-containing refractories. *UNITECR'93 Proceedings*, 32–38.
11. Rymon-Lipinski, T., Reactions of metal additives in magnesia-carbon brick in an oxygen converter (Part 1:the possible reaction sequence in the system MgO–C–Al, MgO–C–Mg, and MgO–C–Si in various atmospheres). *Stahl Eisen*, 1988, **108**(22), 1049–1055.
12. Rymon-Lipinski, T., Reactions of metal additives in magnesia–carbon brick in an oxygen converter, Part 2: formation of metal suboxides and magnesia vapor. *Stahl Eisen*, 1988, **108**(22), 1055–1059.
13. Poirier, J. and Rigaud, M. A., The stability of metals, carbides and oxides in carbon-magnesia refractories. *J. Can. Ceram. Soc*., 1993, **62**(1), 370–376.
14. Mapiravana J., Argent B. B. and Rand B. Reactions of silicon and aluminium in MgO–graphite composites: 2. Reaction products, in UNITECR'93 Proceedings, 1993, 251–253.
15. Brant, P. O. R. C. and Rand, B., Reactions of silicon and aluminium in MgO–graphite composites: 1, Effects on Porosity and Microstructure. *UNITECR'93 Proceedings*, 247–250.
16. Artir, R., Lee, W. E., Argent, B. B. and Larsen, P. H., Reactions of aluminum and silicon in MgO–graphite composites and prediction of phase constitution using MTDATA. *High-Temperature and Materials Science*, 1995, **34**, 69–103.
17. Goto, K., Argent, B. B. and Lee, W. E., Corrosion of MgO–$MgAl_2O_4$ spinel refractory bricks by calcium aluminosilicate slag. *J. Am. Ceram. Soc*., 1997, **80**(2), 3461–3471.
18. Zhang S. and Lee W. E., Interaction between antioxidants and impurities in MgO–C refractories — a thermodynamic study, in preparation.
19. Yamaguchi, A., Control of oxidation-reduction in MgO–-C refractories. *Taikabutsu Overseas*, 1984, **4**(1), 332–337.
20. Yu, J. and Yamaguchi, A., Behaviour of Al on microstructure and properties of MgO–C–Al refractories. *J. Ceram. Soc. Jpn*, 1993, **101**(4), 475–479.
21. Zhang S. and Lee W. E., Influence of additives on corrosion resistance and corroded microstructures of MgO–C refractories. *J. Eur. Ceram. Soc*, in press.